PAPER

$E \times B$ flow driven electron temperature bifurcation in a closed slot divertor with ion $B \times \nabla B$ away from the X-point in the DIII-D tokamak

To cite this article: X. Ma *et al* 2022 *Nucl. Fusion* **62** 126048

IOP Publishing | International Atomic Energy Agency Nuclear Fusion

Nucl. Fusion **62** (2022) 126048 (8pp) https://doi.org/10.1088/1741-4326/ac9743

$E \times B$ flow driven electron temperature bifurcation in a closed slot divertor with ion $B \times \nabla B$ away from the X-point in the DIII-D tokamak

X. Ma[1,*], H.Q. Wang[1,*], H.Y. Guo[2], A. Leonard[1], R. Maurizio[3], E.T. Meier[4], J. Ren[5], P.C. Stangeby[6], G. Sinclair[1], D.M. Thomas[1], R.S. Wilcox[7], J.H. Yu[1] and J. Watkins[8]

[1] General Atomics, PO Box 85608, San Diego, CA 92186-5608, United States of America
[2] ENN Group, Hebei, China
[3] Oak Ridge Associated Universities, 100 ORAU Way, Oak Ridge, TN 37830, United States of America
[4] Zap Energy Inc., Smith Tower, 506 Second Avenue, Seattle, WA 98104, United States of America
[5] University of Tennessee Knoxville, Knoxville, TN 37996, United States of America
[6] University of Toronto, 4925 Dufferin St., Toronto, M3H 5T6, Canada
[7] Oak Ridge National Laboratory, PO Box 2008 Oak Ridge, TN 37831, United States of America
[8] Sandia National Laboratories, Albuquerque, NM, United States of America

E-mail: maxinxing@fusion.gat.com and wanghuiqian@fusion.gat.com

Received 13 July 2022, revised 26 September 2022
Accepted for publication 4 October 2022
Published 31 October 2022

Abstract

An electron temperature bifurcation is observed in the small angle slot divertor, which has been developed to enhance neutral cooling across the divertor target by coupling a closed slot structure with appropriate target shaping. Experiments in the DIII-D tokamak and associated SOLPS-ITER modeling with full drifts find a strong interplay between drifts and divertor geometry on divertor dissipation. The coupling of divertor geometry and drift flows can strongly affect the path towards divertor detachment onset as the plasma density is raised. With the strike point on the inner slanted surface and ion $\mathbf{B} \times \nabla B$ away from the magnetic X-point, bifurcative transitions were observed with sharp decrease of T_e towards detachment onset both experimentally and computationally. This differs from the situation for the open divertor where the T_e cliff was only observed for ion $\mathbf{B} \times \nabla B$ towards the X-point. SOLPS-ITER modeling with full drifts demonstrates that the magnitude of the $\mathbf{E} \times \mathbf{B}$ drift flow is comparable with the main plasma flow. The reversal of both the poloidal and radial $\mathbf{E} \times \mathbf{B}$ flows near the strike point leads to rapid density accumulation right near the separatrix, which results in bifurcative step transition of divertor conditions with cold plasma across the entire divertor target plate. These results indicate that the interplay between geometry and drifts should be fully taken into account in future fusion reactor divertor designs.

Keywords: tokamak, divertor physics, drift, SOLLPS-ITER modeling

(Some figures may appear in colour only in the online journal)

[*] Authors to whom any correspondence should be addressed.

1. Introduction

Development of innovative divertor solutions for robust controls of both heat flux and erosion at targets still remains one of the biggest challenges to the design and operation of next generation high performance steady-state fusion devices. It requires: heat load at the divertor target plate $q_\perp \leqslant 10$–15 MW m^{-2}, and divertor plasma temperature near the target $T_e \leqslant 5$–10 eV to suppress net erosion [1, 2]. Consequently, divertors must be operated with detached plasmas conditions, in which most of the power is dissipated before reaching divertor targets [3–5]. Thus, robust detachment control is essential for future high-power long-pulse tokamaks [6]. For over 20 years, divertor geometry optimization has been extensively explored for enhanced energy and momentum dissipation, with results favoring more closed divertor configurations [7–11]. A small angle slot (SAS) divertor concept has been developed on the DIII-D tokamak based on SOLPS modeling, which combines the effects of a closed slot structure for enhanced neutral trapping inside the divertor and optimized target shaping to tailor the neutral distribution across the entire target surface [12–14]. The first experimental tests and drift-dependent modeling already found a strong interplay between divertor geometry and $\mathbf{E} \times \mathbf{B}$ drift flows on divertor dissipation [15–17], which is not seen in open divertors.

Bifurcation-like confinement transitions in magnetically confined plasmas, in which $\mathbf{E} \times \mathbf{B}$ drift plays an important role, have been widely discussed [18, 19]. Such bifurcative step transition is also observed in the DIII-D lower open divertor for operation with normal-B_T (ion $\mathbf{B} \times \nabla B$ drift pointing towards the magnetic X-point) [20, 21]. The formation of such detachment bifurcation has been associated with impurity radiation loss [22], and anomalous cross-field transport [23, 24]. Recent modeling with full drifts, using 2D boundary plasma codes UEDGE [20] and SOLPS-ITER [25], indicates that the interdependence of the $\mathbf{E} \times \mathbf{B}$ drift flows in the private flux region (PFR), divertor plasma potential and divertor conditions is the main drive for such bifurcation in an open divertor.

Here, we report for the first time a similar bifurcation-like transition in divertor plasma conditions in a closed slot divertor, the SAS divertor. It is found that the path towards detachment can be dramatically altered by varying the position of the strike point relative to the SAS target plate [17]. With the strike point on the inner slanted surface of the SAS divertor, a bifurcative transition was observed with the target T_e suddenly falling below $\sim$5 eV for both toroidal field directions. This differs from the situation for the open divertor configuration where the T_e cliff was only observed for normal-B_T direction. Detailed SOLPS-ITER simulations with full drifts were able to reproduce the T_e cliff with ion $\mathbf{B} \times \nabla B$ drift pointing away from the magnetic X-point, revealing the essential role of $\mathbf{E} \times \mathbf{B}$ drift flows in this bifurcative process. We found that the observed T_e cliff is strongly coupled to the $\mathbf{E} \times \mathbf{B}$ drift flow reversal near the strike point and in the scrape-off layer (SOL) region, which is caused by the non-linear interaction between

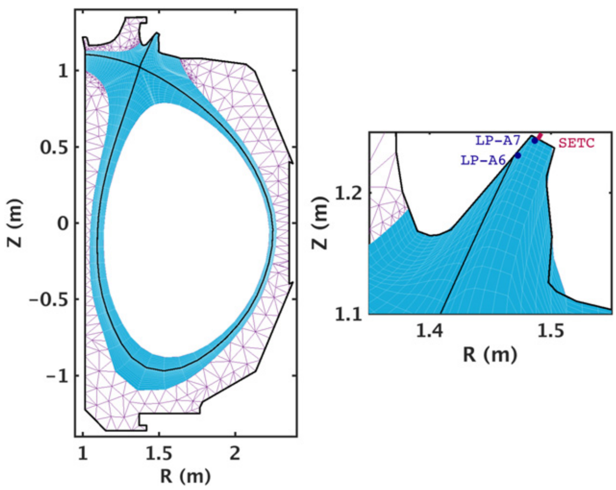

Figure 1. Left: SOLPS-ITER computational mesh used for the modeling with strike point at the inner slanted surface of the SAS divertor. Right: positions of two Langmuir probes (LP-A6 & LP-A7) and one of the surface erosion thermocouples.

$\mathbf{E} \times \mathbf{B}$ drift flows, electron temperature, density, and plasma potential.

The paper is organized as following. Section 2 describes the experiments conducted in the SAS divertor in the DIII-D tokamak and the detailed modeling setups. The experimental data and corresponding modeling results are discussed in section 3. The necessary condition for detachment bifurcation in the modeling is discussed in section 4. Finally, a summary and some conclusions are given in section 5.

2. Experiment and modeling setup

The shape of the cross-section of the SAS divertor in the DIII-D tokamak is shown in figure 1. It consists of a small target angle in the near scrape-off layer (near-SOL) region and a progressive slot opening toward the far-SOL region [13, 14]. Experiments with the outer strike point in the SAS divertor were carried out systematically in H-mode plasma conditions with plasma current, $I_p = 1$ MA, toroidal field, $B_T = 2$ T, neutral beam heating power, $P_{NBI} = 4.0$–4.5 MW, and safety factor $q_{95} \sim 4.75$. There experiments were conducted with three main approaches: density scans until divertor detachment with fixed strike point to investigate the detachment physics; switching toroidal field direction to investigate the influence of $\mathbf{E} \times \mathbf{B}$ drifts on the trajectories towards detachment onset; strike point sweeping to examine the interplay between divertor geometry and $\mathbf{E} \times \mathbf{B}$ drift flows. A complete set of boundary diagnostics were utilized in these experiments, including multiple-channel Thomson scattering (TS) system for upstream electron density and temperature profile measurements, target embedded Langmuir probes (LPs) to measure the electron density, temperature, particle flux and inferred heat flux along the divertor target plates, and surface eroding thermocouples (SETCs) to access the heat flux striking the divertor target.

Although the electron temperature bifurcation was observed in both toroidal field directions. This paper will only focus on the experiments and corresponding modeling with ion $\mathbf{B} \times \nabla B$ away from the magnetic X-point and the strike point on the inner slanted surface of SAS. The modeling with opposite field direction has not fully reproduced experimental results, specifically the bifurcative transition in divertor plasma conditions. This modeling work is still ongoing and the drifts are expected to play an important role as well [26, 27].

Drift-dependent modeling of the experimental discharges was performed for a better understanding of the physics involved, using the state-of-the-art boundary plasma code package, SOLPS-ITER [28], the coupled version of the 2D multi-fluid transport code B2.5 [29] and the 3D kinetic neutral transport code EIRENE [30]. The B2.5 fluid code computes the background plasma by solving the 2D Braginskii equations, and provides the solutions to EIRENE. Then EIRENE computes and returns the source and sink terms for plasma particles, momentum and energy due to plasma–neutral interactions. In this paper, the simulations were carried out for a deuterium (D) plasma with carbon (C) wall and targets. Simulated particles in the modeling include ions ($D^+, C^+, C^{+2}, C^{+3}, C^{+4}, C^{+5}, C^{+6}$), atoms (D, C) and molecules (D_2). A complete set of atomic and molecular reactions are accounted for in the modeling, including neutral–neutral collisions. All particle drifts, $\mathbf{E} \times \mathbf{B}$, $\mathbf{B} \times \nabla B$, viscosity and the associated currents are activated in the modeling.

The computational mesh used in the modeling for the B2.5 code has a resolution of 96×32 and is constructed using the real EFIT [31] plasma equilibrium of shot 179748 at 4000 ms, as shown in figure 1. Triangular meshes for the EIRENE code are also shown in figure 1. The outer strike point is placed at the inner slanted surface of the SAS divertor. The solid structure geometry represents first wall surfaces of the present DIII-D tokamak, including the SAS divertor. The narrow structure of the SAS divertor makes it difficult to reproduce actual DIII-D boundary conditions. As a result, an extended computational mesh is implemented, in which a slight modification to the SAS lower outer corner is made by including a more progressive opening [32]. At the core-edge interface, the total power flux is set to 4 MW, shared equally by ions and electrons, to match the power crossing the separatrix for the modeled discharge. A leakage boundary condition is set at the B2.5 grid boundaries for the PFR and common flux region [33]. A sheath boundary condition is adapted at the boundary of both inner and outer targets, with $V_{\dagger t} + \boldsymbol{V}_{E\times B} \cdot \vec{\boldsymbol{B}}/B = c_s \times$ [34], where $V_{\dagger t}$ is the parallel plasma flow speed at the target, and $c_s = \sqrt{k_B(T_e + T_i)/m_i}$, the plasma isothermal sound speed. T_i and m_i are the ion (D+) temperature and mass respectively. Plasma flux leaving the B2.5 grid boundary is recycled as neutral atoms. The recycling coefficients are set to be 100% at the targets and 99% at the SOL boundary respectively. For carbon sputtering, both the physical sputtering with Roth–Bodhansky yields [35] and the chemical sputtering with a fixed 2% yield are included in the modeling.

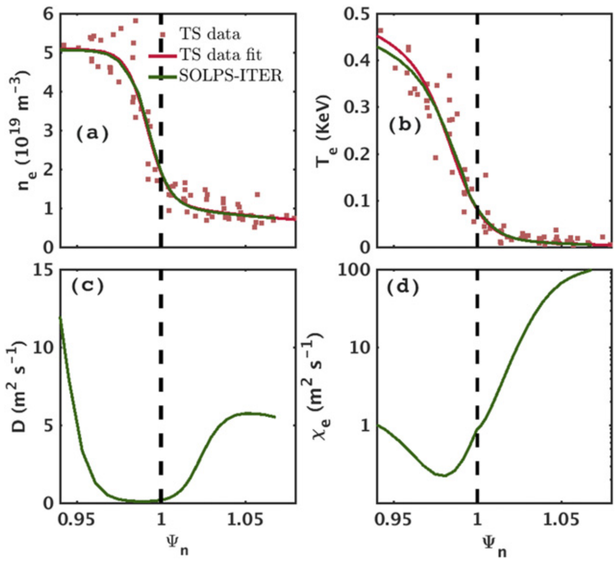

Figure 2. Electron density (*a*) and temperature (*b*) profiles at the outer midplane measured by a TS system (red dot) for shot 179838 at 4900 ms, fitted by a modified hyperbolic function (red solid line), and from corresponding SOLPS-ITER simulation (green solid line). (*c*) and (*d*) Anomalous cross-field transport coefficient (particle diffusivity D, and electron thermal diffusivity χ_e) profiles at the outer midplane determined by the fitting procedure.

The anomalous cross-field transport coefficients used in the modeling are determined by matching the outer mid-plane (OMP) electron density and temperature profiles from the simulation with experimentally measured upstream profiles from the TS system. In this process, the values of particle diffusivity D and electron thermal diffusivity χ_e are iterated until a satisfactory match is achieved [36]. The ion thermal diffusivity, χ_i, is set to be equal to χ_e, due to the absence of reliable measurements of ion temperature in the SOL region. The calculation was performed using experimental measurements from shot 179838 at 4900 ms with an averaged plasma density $\overline{n}_e \approx 5.0 \times 10^{19}$ m^3. Figures 2(*a*) and (*b*) show measured electron density and temperature data (red dots) at the outer midplane, along with fitted profiles (red solid lines) using a modified hyperbolic function. Profiles from simulations are overplotted with green lines. Here ψ_n is the normalized poloidal magnetic flux coordinate, defined as $\psi_n = \sqrt{(\psi - \psi_0)/(\psi_1 - \psi_0)}$ with ψ the poloidal magnetic flux and ψ_0 and ψ_1 the poloidal flux at the magnetic axis and at the X-point, respectively. A good match between experimental profiles and those from simulations was obtained after a few iterations. The calculated cross-field transport coefficient profiles at the outer midplane are shown in figures 2(*c*) and (*d*). Both profiles show a well-like shape with minimum values near the separatrix, which is consistent with observations in H-mode plasmas in DIII-D [16, 37]. In the divertor region below the X-point, both the particle diffusion and thermal diffusion coefficients are set to be constant across the computational cells, with $D = 0.18$ m^2 s^{-1} and $\chi_e = \chi_i = 0.9$ m^2 s^{-1}. These values are taken to be the same as that at the separatrix ($\psi_n = 1$) of the calculated profiles in figures 2(*c*) and (*d*).

3. Results

Figures 3(*a*)–(*c*) show the electron temperature, T_e, and the particle flux, J_{sat}, near the strike point ($\psi_n = 1.0005$) measured by target Langmuir probe LP-A6, and deposited heat flux, $q_\perp$, at the slot bottom of the SAS divertor ($\psi_n = 1.002$) inferred from Langmuir probe LP-A7 and measured by surface thermocouples (SETC), as a function of the upstream OMP separatrix density, $n_{e,sep}$. The experimental data is taken from shot 179838 in the DIII-D experimental campaign FY2019. The ratio between $n_{e,sep}$ and $\overline{n}_e$, the line averaged density, $\alpha = n_{e,sep}/\overline{n}_e$ varies depending on the plasma condition, and typically increases with $\overline{n}_e$. Here, automated fits of the pedestal density profiles measured by the TS system were used to assess the actual values of $n_{e,sep}$. A subset of detailed profile fits in the time range were adjusted to have more reliable separatrix locations based on a power balance estimate [38]. Several values of the ratio based on these fittings and adjustments are shown in table 1. But uncertainties still exist due to the scattering of the data points. As an estimation, a linear relation is obtained: $\alpha = 0.051\times\overline{n}_e + 0.11$. This formula is used to transform experimental measured $\overline{n}_e$ to $n_{e,sep}$, so that the modeling results can be compared to the modeling outcome since SOLPS-ITER only provides $n_{e,sep}$ value.

As shown in the figure, for ion $\mathbf{B} \times \nabla B$ away from the X-point, the divertor plasma enters the highly dissipative regime above $n_{e,sep} \sim 1.85 \times 10^{19}$ m^{-3}, as marked by a sharp decrease in T_e near the strike point, from around 15 eV to 5 eV. The particle flux to the target near the strike point shows a more complex dynamic. As upstream density increases, the J_{sat} value increases until it reaches a maximum value. Then the particle flux decreases and reaches the minimum value, followed by a sharp increase, at the same $n_{e,sep}$ where the T_e cliff occurs. The evolution of particle flux to the target is mostly due to the changing of $\mathbf{E} \times \mathbf{B}$ drift fluxes near the strike point, which will be discussed in later section. The deposited heat flux at the bottom of the slot continues to drop with increasing upstream density until the detachment onset of the divertor plasma. However, the heat flux measured by the thermocouple is significantly larger than that inferred from the Langmuir probe, especially near electron temperature bifurcation. This is due to the fact that thermocouples receive extra heat load due to radiative heating, while LP only infer heat flux from ions. Similar experiments were conducted in the DIII-D campaign FY2020. To check the consistency of the results, experimental data from shot 185884 in FY2020 is also shown in figure 3. The results are fairly reproducible, except the T_e cliff happened at a slightly higher upstream density.

SOLPS-ITER simulation with full drifts successfully predicts the electron temperature bifurcation. The results are overplotted with solid green lines in figure 3. The modeling did not cover the whole range of the density from the experiment. The focus of this paper is to provide insights on the divertor plasma behavior near the electron temperature bifurcation. It is seen that the modeling is able to qualitatively reproduce the overall trends and key features of the experimental measurements from LP and thermal couples. But it is important to note that

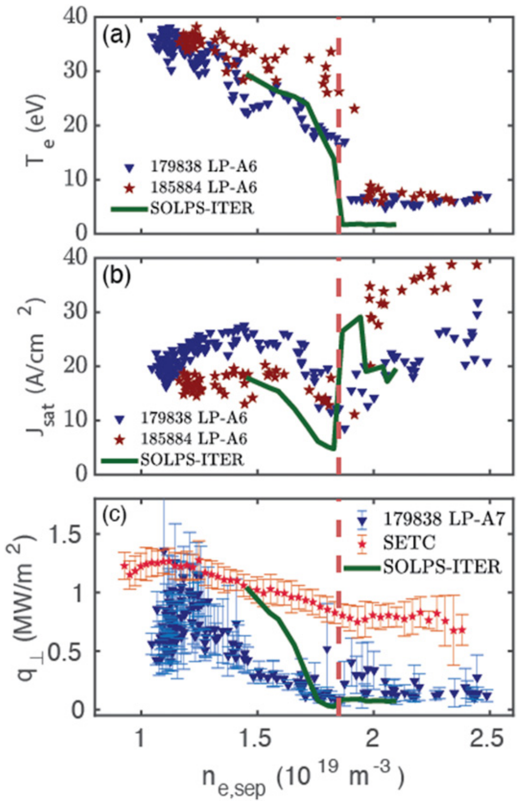

Figure 3. (*a*) Electron temperature, T_e, and (*b*) particle flux, J_{sat}, near the strike point with $\psi_n = 1.0005$, measured by Langmuir probe (LP-A6) embedded in the divertor target plate, (*c*) deposited heat flux, $q_\perp$, at the slot bottom with $\psi_n = 1.002$ inferred from Langmuir probe LP-A7 and measured by SETCs on the target, versus $n_{e,sep}$, the upstream OMP separatrix density. Electron temperature, particle flux and deposited heat flux at corresponding locations from SOLPS-ITER modeling are overplotted with solid lines. The dashed vertical red line marks the position where the bifurcation happens.

the divertor plasma is more detached with T_e around 2 eV in the modeling, indicating the occurring of volume recombination near the target. While the experimental data shows moderate detachment state with $T_e \sim 5$ eV. The deposited heat flux, $q_\perp$, from the modeling without contribution from radiation, is also significantly lower (factor of 2–4) than thermocouple measurements.

To investigate the mechanism of such bifurcation behavior of the plasma, the profile evolution along the outer target of several plasma quantities including the electron temperature, density and neutral density from the SOLPS-ITER modeling is shown in the left side of figure 4. Three simulation cases are shown here with increasing upstream densities (pre-T_e drop : $n_{e,sep} = 1.76 \times 10^{19}$ m^{-3}, at $-$ T_e drop : $n_{e,sep} = 1.83 \times 10^{19}$ m^{-3}, post $-$ T_e drop : $n_{e,sep} = 1.86 \times 10^{19}$ m^{-3}). It is seen that as the upstream density increases, the electron temperature decreases as expected until a sudden collapse with $T_e \sim 2$ eV along the whole target. In the meantime, the electron temperature gradient decreases as well. Significant increases of the plasma density and neutral density in the SOL region are also observed.

SOLPS-ITER finds that the electron temperature bifurcation is strongly associated with an $\mathbf{E} \times \mathbf{B}$ flow reversal in

Table 1. Ratio of $n_{\mathrm{e,sep}}$ to $\overline{n}_{\mathrm{e}}$ based on pedestal profile fittings and separatrix adjustments using TS data for shot 179838.

$\overline{n}_{\mathrm{e}}(10^{19}\ \mathrm{m}^{-3})$	3.70	3.85	4.18	4.55	5.07
$n_{\mathrm{e,sep}}(10^{19}\ \mathrm{m}^{-3})$	1.1	1.21	1.35	1.55	1.88
α	0.29	0.31	0.32	0.34	0.37

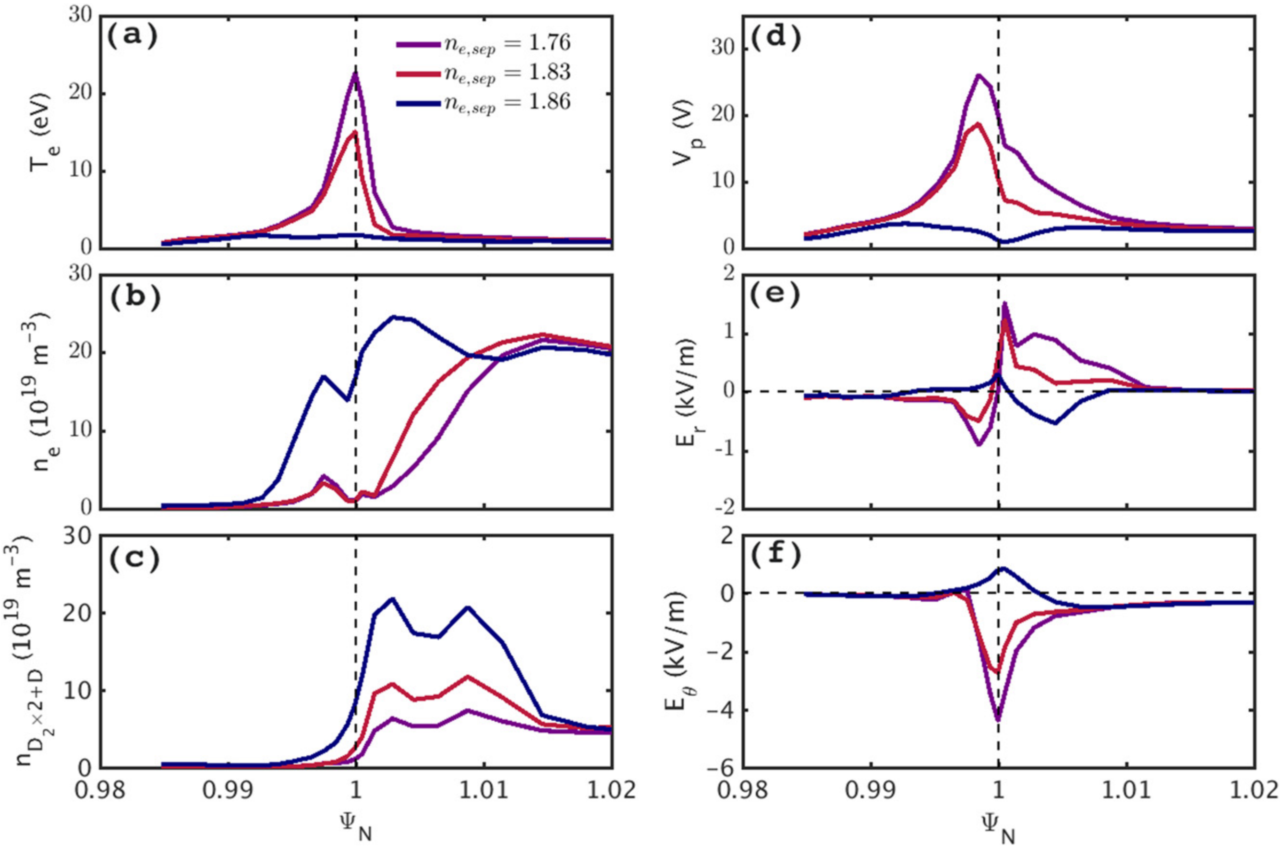

Figure 4. Radial profiles of (*a*) electron temperature, T_{e}, (*b*) electron density, n_{e}, (*c*) neutral density, $n_{\mathrm{D}} + n_{\mathrm{D_2}} \times 2$, (*d*) plasma potential, V_{p}, (*e*) radial electric field, E_r, (*f*) poloidal electric field, E_θ, along the outer target of the SAS divertor for three SOLPS-ITER simulation cases with increasing upstream separatrix density near the bifurcation.

the SOL region. The right side of figure 4 show radial profiles of plasma potential, radial and poloidal electric fields. Here, the plasma potential, V_{p}, was calculated by the SOLPS-ITER code which included the effect of the current density along the magnetic field lines, on the sheath potential and on Ohm's law. The radial and poloidal electric field are calculated using the plasma potential: $E_r = -\frac{\partial \mathbf{V_P}}{\partial \boldsymbol{r}}$, $E_\theta = -\frac{\partial \mathbf{V_P}}{\partial \boldsymbol{\theta}}$. Here, r and θ represent the radial and poloidal distance variance, respectively. As show in figure 4(*d*), the radial profile of the plasma potential largely follows the radial variation of T_{e}. In attached conditions with $T_{\mathrm{e}} > 15$ eV, the radial electric field, E_r, causes a strong poloidal $\mathbf{E} \times \mathbf{B}$ flow away from the target in the SOL region, maintaining a low density, high temperature state. As upstream density increases, plasma potential and its radial gradient start decreasing. Thus, E_r decreases as well, along with decreased poloidal $\mathbf{E} \times \mathbf{B}$ flow out of the divertor, which facilitates accumulation of particles near the strike point and further reduction of the electron temperature. This positive feedback process initiated nonlinear evolution of the electron density and temperature in the outer divertor, and eventually leads to reversal of E_r and poloidal $\mathbf{E} \times \mathbf{B}$ flow, changing its direction from away from the target plate to towards the target plate.

Similar flow reversal is also observed from the modeling for the radial $\mathbf{E} \times \mathbf{B}$ flux. The poloidal electric field, E_θ, in the SOL region [39–41] is also given by equation (1)

$$E_\theta = -\frac{\partial V_{\mathrm{p}}}{\partial \theta} = \frac{B_{\mathrm{tot}}}{B_\theta}\left(\frac{j_\dagger}{\sigma_\dagger} - \frac{0.71}{e}\frac{\partial T_{\mathrm{e}}}{\partial s_\dagger} - \frac{1}{ne}\frac{\partial p_{\mathrm{e}}}{\partial s_\dagger}\right). \quad (1)$$

Here, $j_\dagger$ is the parallel current density, $s_\dagger$ is the parallel distance along the field lines. B_{tot} and B_θ represent the total and poloidal magnetic fields respectively. p_{e} gives the electron pressure. The plasma resistivity is $\sigma_\dagger$ (ohm^{-1} m^{-1}) $\approx 3.6 \times 10^7$ $[T_{\mathrm{e}}\ (\mathrm{keV})]^{\frac{3}{2}}$ [37]. E_θ is determined by three terms, the parallel current (usually neglected in attached conditions), the parallel gradient of electron temperature and the parallel gradient of electron pressure. The contribution of the three components

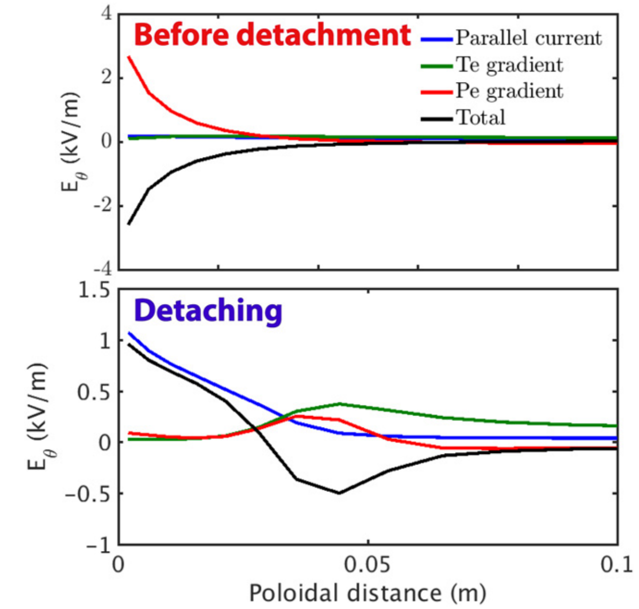

Figure 5. Poloidal electric field, E_θ, along the flux tube in SOL near the strike point due to parallel current, electron temperature gradient and pressure gradient for both attached and detaching conditions corresponding to the $n_{e,sep} = 1.83$ and 1.86×10^{19} m^{-3} cases. The poloidal distance starts from the outer target.

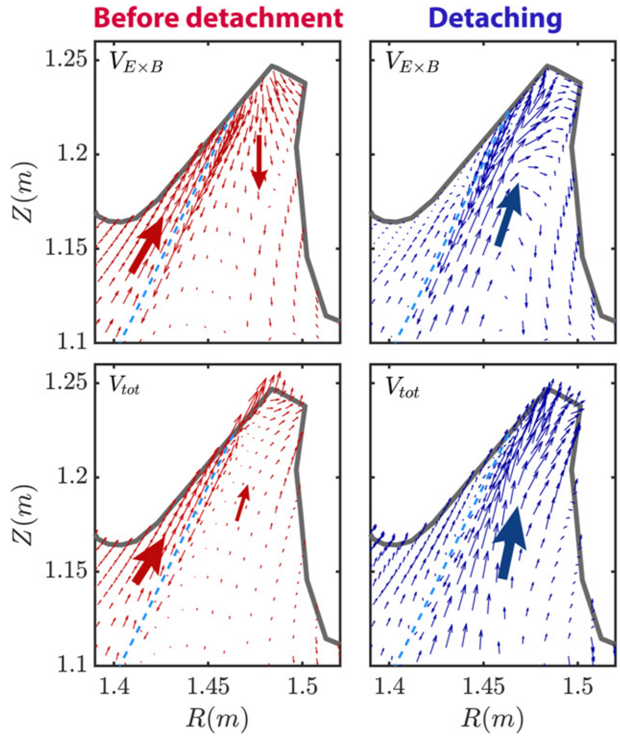

Figure 6. Ion $\mathbf{E} \times \mathbf{B}$ velocity, $V_{E\times B}$, and ion total velocity, V_{tot}, distribution for attached and detached conditions. The size of the arrows indicates the relative magnitude of the velocity.

along the flux tube near the strike point for both attached and detached plasmas ($n_{e,sep} = 1.83$ and 1.86×10^{19} m^{-3}) is shown in figure 5. It is seen that before detachment, the poloidal electric field near the target due to parallel current and electron temperature gradient can be neglected. The pressure gradient term results in negative E_θ and radial $\mathbf{E} \times \mathbf{B}$ flow away from the target plate. As plasma density increases, electron temperature drops. Since $\sigma_\dagger \sim T_e^{3/2}$, the first term with parallel current increases. In the meanwhile, the pressure gradient term decreases with increased density. Thus, the magnitude of E_θ decreases and eventually reverses its direction, causing the reversal of radial $\mathbf{E} \times \mathbf{B}$ flow, from away from the target plate to towards the target plate, similar to the poloidal $\mathbf{E} \times \mathbf{B}$ flow.

Furthermore, the $\mathbf{E} \times \mathbf{B}$ flow reversal during the divertor plasma detaching process can be clearly seen from the velocity vector plots. Figure 6 shows the comparison of the ion $\mathbf{E} \times \mathbf{B}$ velocity, $V_{E\times B}$, and the total velocity, V_{tot}, for two cases near the T_e cliff. Here the ion total velocity includes the $\mathbf{E} \times \mathbf{B}$ velocity, poloidal projection of the ion parallel velocity and other velocities (diamagnetic velocity, magnetic field curvature velocity, etc). Generally, the poloidal component of the $\mathbf{E} \times \mathbf{B}$ velocity dominates. As shown in the left side of figure 6, before detachment, $V_{E\times B}$ is towards the target in the PFR and away from the target in the near-separatrix part of the SOL region, which is in the opposite direction of the main plasma flow, resulting in smaller total plasma flow towards the target. In contrast, for the low T_e condition, the $V_{E\times B}$ flow in the near-separatrix part of the SOL region reverses its direction, going in the same direction as the main plasma flow, resulting in much larger total plasma flow into the divertor, as shown in the right side of figure 6. It is clear that the drift flow is comparable to the main plasma flow. The reversal of

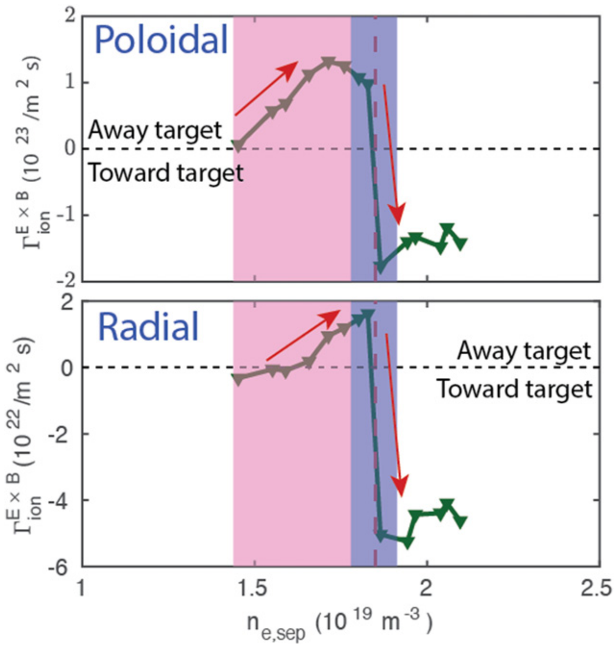

Figure 7. Poloidal (upper) and radial (lower) $E \times B$ flux, near the strike point, calculated from SOLPS-ITER simulations, versus $n_{e,sep}$. The dashed vertical red line marks the position where the bifurcation happens.

$\mathbf{E} \times \mathbf{B}$ flows allows a rapid density accumulation in the SOL region, especially in the divertor slot, initiating detachment and leading to plasma cooling across the entire outer target. As a result, the divertor plasma shows a bifurcative step transition from low-density, high-temperature, attached conditions to high-density, low-temperature, detached conditions, as shown in both experiments and modeling.

The evolution of particle flux in figure 3(*b*) is more complex and can be inferred from the dynamics of the poloidal and radial $\mathbf{E} \times \mathbf{B}$ drift fluxes in the SOL region near the strike point as shown in in figure 7. It is important to note that the amplitude of the poloidal drift flux is nearly one order larger than the radial drift flux. For attached conditions, both poloidal and radial $\mathbf{E} \times \mathbf{B}$ fluxes are away from the divertor plate. As upstream density increases, their amplitudes also increase, leading to decreased total particle flux to the target plates as shown in figure 3(*b*). When the electron temperature starts dropping, the poloidal $\mathbf{E} \times \mathbf{B}$ flux decreases and reveres its direction eventually, from away from the target to towards the target. Combined with reversal of the radial $\mathbf{E} \times \mathbf{B}$ flux, a significant increase (factor of 3–4) of the total particle flux to the target is observed. This is clear evidence that $\mathbf{E} \times \mathbf{B}$ drift flows are comparable with the main plasma flow, and can strongly affect the particle recycling in the divertor region.

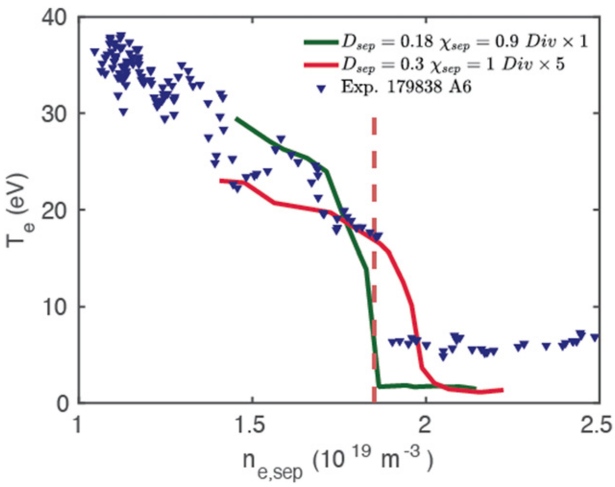

Figure 8. Electron temperature near the strike point measured by target Langmuir probe (LP-A6) and two sets of SOLPS-ITER simulations with different cross-field transport coefficients, as a function of upstream OMP separatrix density. The dashed vertical red line marks the position where the bifurcation happens.

4. Necessary conditions for detachment cliff

For the entire set of simulations discussed above, the same set of radial transport coefficient is used. To investigate the influence of the plasma profile on the impact of drifts, different set of radial transport coefficient is calculated using measured upstream n_e and T_e profiles at lower density ($\overline{n}_e \approx 4.0 \times 10^{19}$ m^3) of shot 179838 at 3800 ms. Again, particle diffusivity D and electron thermal diffusivity χ_e are iterated until a satisfactory match between experimental and modeling profiles is achieved. Larger radial transport at the separatrix is achieved, with $D_{sep} = 0.3$ m^2 s^{-1} and $\chi_{sep} = 1.0$ m^2 s^{-1}. In addition, the transport coefficients in the divertor region need to be increased by a factor of 5 for a better match to the n_e and T_e profiles along the target. Stronger radial transport in the divertor region leads to larger SOL width and broader profiles compared to the set of modeling discussed in the first part of the manuscript. Consequently, smaller radial gradient leads to weaker $\mathbf{E} \times \mathbf{B}$ drift effects. The resulting target electron temperature as a function of the upstream density is compared to the previous results, as shown in figure 8. It is seen that the evolution of the electron temperature at the target shows a less dramatic bifurcation. It is clear that formation of such T_e cliff on a highly slanted surface favors a relative narrow SOL width with strong radial gradient near the separatrix. This result is consistent with modeling analysis of necessary conditions for a T_e cliff in the lower divertor of DIII-D with full drifts [25].

5. Conclusion

In summary, experiments in the DIII-D SAS divertor and associated SOLPS-ITER modeling with full drifts find a strong synergy between drifts and divertor geometry on divertor dissipation. The coupling of divertor geometry and drift flows can strongly affect the path towards divertor detachment onset. With strike point on the inner slanted surface of the SAS divertor and ion $\mathbf{B} \times \nabla B$ away from the magnetic X-point, an electron temperature bifurcation is observed with T_e suddenly falling below ~5 eV both experimentally and computationally. This differs from the situation for the open divertor where the T_e cliff was only observed for ion $\mathbf{B} \times \nabla B$ towards the magnetic X-point, and the non-linear evolution of the poloidal $\mathbf{E} \times \mathbf{B}$ drift flows in the PFR plays a key role. The cause of the T_e bifurcation in the SAS divertor is different and is mainly due to the $\mathbf{E} \times \mathbf{B}$ flow reversal in the SOL region. SOLPS-ITER modeling with full drifts shows that the $\mathbf{E} \times \mathbf{B}$ drift flows are comparable with the main plasma flow. Before divertor detachment, as the upstream density increases, the divertor electron temperature decreases. $\mathbf{E} \times \mathbf{B}$ drift flows that are away from the divertor plate decrease as well, leading to a rapid accumulation of particles in the slot. Electron temperature near the strike point is further reduced until the $\mathbf{E} \times \mathbf{B}$ drift flows eventually reverse, changing the direction from away from the target plate to towards the target plate. Enhanced total plasma flow into the divertor results in sudden collapse of the electron temperature, driving divertor plasma towards detachment. What is more, such step-like transition can also be observed with ion $\mathbf{B} \times \nabla B$ towards the magnetic X-point in the SAS divertor. Detailed SOLPS-ITER modeling is still ongoing to investigate the mechanism behind this. These results indicate that the interplay between geometry and drifts needs to be fully taken into account in future fusion reactor divertor designs.

Disclaimer

Acknowledgments

This material is based upon work supported by the US Department of Energy, Office of Science, Office of Fusion Energy Sciences, using the DIII-D National Fusion Facility, a DOE Office of Science user facility, under Award(s) DE-FC02-04ER54698, DE-SC0019256, DE-AC05-00OR22725 and DE-NA0003525.

ORCID iDs

X. Ma https://orcid.org/0000-0002-7326-2146
H.Q. Wang https://orcid.org/0000-0003-1920-2799
A. Leonard https://orcid.org/0000-0001-9356-1074
R. Maurizio https://orcid.org/0000-0001-9896-6732
P.C. Stangeby https://orcid.org/0000-0002-3511-2286
G. Sinclair https://orcid.org/0000-0003-4195-177X
R.S. Wilcox https://orcid.org/0000-0003-1369-1739

References

[1] Stangeby P.C. and Leonard A.W. 2011 *Nucl. Fusion* **51** 063001
[2] Stangeby P.C. 2018 *Plasma Phys. Control. Fusion* **60** 044022
[3] Leonard A.W. 2018 *Plasma Phys. Control. Fusion* **60** 044001
[4] Pitts R. *et al* 2019 *Nucl. Mater. Energy* **20** 100696
[5] Kukushkin A.S., Pacher H.D., Kotov V., Pacher G.W. and Reiter D. 2011 *Fusion Eng. Des.* **86** 2865
[6] Eldon D. *et al* 2017 *Nucl. Fusion* **57** 066039
[7] Lipschultz B. *et al* 1997 *Proc. 16th IAEA Fusion Energy Conf.* (Montreal, Canada 7–11 October 1996) (https://www.iaea.org/publications/5092/fusion-energy-1996-proceedings-of-an-international-conference-in-montreal-canada-7-11-october-1996)
[8] Monk R.D. (JET Team) 1999 *Nucl. Fusion* **39** 1751
[9] Joffrin E. *et al* 2017 *Nucl. Fusion* **57** 086025
[10] Kallenbach A. *et al* 1999 *Nucl. Fusion* **39** 901
[11] Asakura N. *et al* 1999 *J. Nucl. Mater.* **266–269** 182
[12] Guo H.Y., Sang C.F., Stangeby P.C., Lao L.L., Taylor T.S. and Thomas D.M. 2017 *Nucl. Fusion* **57** 044001
[13] Sang C., Guo H.Y., Stangeby P.C., Lao L.L. and Taylor T.S. 2017 *Nucl. Fusion* **57** 056043
[14] Stangeby P.C. and Sang C. 2017 *Nucl. Fusion* **57** 056005
[15] Guo H.Y. *et al* 2019 *Nucl. Fusion* **59** 086054
[16] Casali L., Osborne T.H., Grierson B.A., McLean A.G., Meier E.T., Ren J., Shafer M.W., Wang H. and Watkins J.G. 2020 *Phys. Plasmas* **27** 062506
[17] Ma X., Wang H.Q., Guo H.Y., Stangeby P.C., Meier E.T., Shafer M.W. and Thomas D.M. 2021 *Nucl. Fusion* **61** 054002
[18] Itoh S.I. and Itoh K. 1988 *Phys. rev. Lett.* **60** 2276
[19] Wagner F. 2007 *Plasma Phys. Control. Fusion* **49** B1
[20] Jaervinen A.E. *et al* 2018 *Phys. Rev. Lett.* **121** 075001
[21] Jaervinen A.E. *et al* 2020 *Nucl. Fusion* **60** 056021
[22] Feng Y., Sardei F., Grigull P., McCormick K., Kisslinger J., Reiter D. and Igitkhanov Y. 2002 *Plasma Phys. Control. Fusion* **44** 611–625
[23] Pshenov A.A., Kukushkin A.S. and Krasheninnikov S.I. 2017 *Phys. Plasmas* **24** 072508
[24] Krasheninnikov S.I., Kukushkin A.S., Pshenov A.A., Smolyakov A.I. and Zhang Y. 2017 *Nucl. Mater. Energy* **12** 1061–1066
[25] Du H., Zheng G., Guo H., Jaervinen A.E., Duan X., Bonnin X., Eldon D. and Wang D. 2020 *Nucl. Fusion* **60** 046028
[26] Du H., Guo H.Y., Stangeby P.C., Bonnin X., Zheng G., Duan X. and Xu M. 2020 *Nucl. Fusion* **60** 126030
[27] Maurizio R. *et al* 2021 *Nucl. Fusion* **61** 116042
[28] Bonnin X., Dekeyser W., Pitts R., Coster D., Voskoboynikov S. and Wiesen S. 2016 *Plasma Fusion Res.* **11** 1403102
[29] Schneider R. *et al* 2006 *Contrib. Plasma Phys.* **46** 3
[30] Reiter D., Baelmans M. and Börner P. 2005 *Fusion Sci. Technol.* **47** 172
[31] Lao L., St. John H., Stambaugh R.D., Kellman A.G. and Pfeiffer W. 1985 *Nucl. Fusion* **25** 1611
[32] Ma X., Abrams T., Covele B., Elder J.D., Guo H.Y., Guterl J. and Stangeby P.C. 2020 *Phys. Scr.* **T171** 014072
[33] Meier E. *et al* 2020 *Contrib. Plasma Phys.* **60** e201900151
[34] Chankin A.V., Corrigan G., Groth M. and Stangeby P.C. 2015 *Plasma Phys. Control. Fusion* **57** 095002
[35] Bohdansky J., Roth J. and Bay H.L. 1980 *J. Appl. Phys.* **51** 2861
[36] Canik J.M., Maingi R., Soukhanovskii V.A., Bell R.E., Kugel H.W., LeBlanc B.P. and Osborne T.H. 2011 *J. Nucl. Mater.* **415** S409–12
[37] Canik J.M., Briesemeister A.R., McLean A.G., Groth M., Leonard A.W., Lore J.D. and Moser A. 2017 *Phys. Plasmas* **24** 056116
[38] Leonard A.W., McLean A.G., Makowski M.A. and Stangeby P.C. 2017 *Nucl. Fusion* **57** 086033
[39] Rognlien T.D., Ryutov D.D., Mattor N. and Porter G.D. 1999 *Phys. Plasmas* **6** 1851
[40] Stangeby P.C. 2000 *The Plasma Boundary of Magnetic Fusion Devices* (London: Taylor and Francis)
[41] Braginskii S.I. 1965 *Reviews in Plasma Physics* vol 1 ed M.A. Leontovich (New York: Consultants Bureau) p 205